Radiation boundary conditions for the numerical solution of the 3D time-dependent Schrödinger equation with a localized interaction.

M. Heinen*
Institute of Solid State Research,
Soft Condensed Matter,
Research Centre Jülich,
52425 Jülich, Germany

H.-J. Kull†
Institute of Theoretical Physics A,
RWTH Aachen University,
Templergraben 55, 52056 Aachen, Germany
(Dated: April 29, 2009)

Exact radiation boundary conditions on the surface of a sphere are presented for the single-particle time-dependent Schrödinger equation with a localized interaction. With these boundary conditions, numerical computations of spatially unbounded outgoing wave solutions can be restricted to the finite volume of a sphere. The boundary conditions are expressed in terms of the free-particle Green-function for the outside region. The Green-function is analytically calculated by an expansion in spherical harmonics and by the method of Laplace transformation. For each harmonic number a discrete boundary condition between the function values at adjacent radial grid points is obtained. The numerical method is applied to quantum tunneling through a spherically symmetric potential barrier with different angular momentum quantum numbers l. Calculations for $l = 0$ are compared with exact theoretical results.

PACS numbers: 02.60.Lj, 31.15.-p, 32.80.-t

I. INTRODUCTION

For more than 40 years, finite-difference techniques have been an important tool for the study of time-dependent quantum systems in atomic and molecular physics [1–3]. One of the most basic finite-difference methods for the time-dependent Schrödinger equation (TDSE) was introduced by Goldberg, Schey and Schwartz to demonstrate time-dependent wavepacket scattering from 1D model-potentials [1]. This method has been based on an implicit time-propagation scheme, originally proposed for the heat flow equation by Crank and Nicolson [4]. For the study of more realistic quantum systems advanced techniques for multi-dimensional computations have been developed. These include e.g. alternating-direction-implicit (ADI) methods [5–7], split-operator and fast Fourier transform (FFT) methods [8, 9], mixed finite-difference/harmonic expansion methods [10–13] and B-spline methods [7, 14].

One of the limitations of numerical computations arises from the finite size of the computational grid. Spatially unbounded solutions have to be represented on a necessarily finite computational domain. For this purpose, one often uses periodic, absorbing or rigid-wall boundary conditions. Rigid-wall boundary conditions limit the time evolution up to the arrival of the wavefunction at the grid-boundaries. While periodic boundary conditions are very useful for many-particle systems, absorbing boundary conditions are more commonly applied to isolated single- or few-particle systems. Absorbing boundaries can be achieved by suitably chosen complex potentials [15, 16] or complex coordinates [17]. However, artificial damping of the wavefunction at the boundaries is not a perfect choice because the shape and the extent of the absorber have to be adapted to the approaching wavefunction in order to minimize unavoidable residual reflections. Moreover, if the absorber is not chosen properly the resulting reflections lead to a dissipation of information about the solution exterior to the absorber.

In this paper, we follow a different approach which has attracted more and more interest over the past years. A Green-function method is used to gain the boundary conditions for outgoing waves. These boundary conditions are exact but they are in general nonlocal in space and time. Such boundary conditions are familiar from electrodynamics [18] and by analogy, we call them radiation boundary conditions. They are also known as transparent, outgoing wave, non-reflecting or integral boundary conditions. In previous work it was shown, that radiation boundary conditions can be expressed in terms of the Green-function of a free particle in the asymptotic outside region [19]. The Green-function method has also been treated in some detail in [20, 21]. In [21] semiclassical approximations to the asymptotic Green-function in the presence of a laser field have been given. Other approaches to boundary-free propagation of solutions of the TDSE have also been discussed [22]. Up to now radiation boundary conditions have been mostly applied to 1D

*m.heinen@fz-juelich.de
†kull@ilt-extern.fraunhofer.de

problems and different forms of discrete representations have been gained for that purpose [19–21]. Discrete radiation boundary conditions in 1D and occasionally in 2D have also been a subject of continuing research in applied mathematics [23–28].

In the present work, it is our goal to derive the exact form of the radiation boundary conditions in three dimensions on the surface of a sphere. The sphere is introduced here as an artificial boundary between a 3D quantum system and its surrounding region. Such a separation is based on the assumption that the potential and the initial wave function can be completely localized within a sphere. For long-range potentials the treatment will be less accurate, although satisfactory results may still be obtained if the radius of the sphere is chosen sufficiently large. The basic difference between previous 1D and the present spherical 3D problem is the fact that for a non-zero angular momentum quantum number l, the radial motion is governed by an effective potential $l(l+1)/2r^2$ with a range $r = \mathcal{O}(l)$. For sufficiently large angular momentum quantum numbers, it is therefore essential to include the effective potential in the calculation of the Green-function. In this work we present an exact solution of this problem that is based on the method of Laplace transformation and an expansion of the Laplace-transformed Green-function in partial fractions. Similar methods have been used in [29] for the 3D hyperbolic wave equation.

For a quantum state with angular momentum quantum number l, the resulting boundary condition is expressed as a sum of $l+1$ convolution integrals in time. For a large radius of the computational domain one obtains asymptotically the 1D result [19]. The present result is a generalization that is exact for arbitrary radii. For large values of l, the Green-function of the system (*i.e.* the sum of the convolution kernels) decays very fast in time. This means that one may truncate the time interval for the convolution integrals, thereby reducing the expense for each timestep n from linearly rising with n to constant. Due to the shorter relaxation times for larger quantum numbers l the numerical effort of the method actually gets reduced with increasing complexity of the wavefunction.

As an example, we study the problem of spontaneous quantum decay of a particle in a spherically symmetric potential well with finite range. Recently, the problem of spontaneous quantum tunneling has received renewed attention and exact theoretical results for the tunneling of spherical S-waves have been reported. We show that the present numerical method is able to accurately reproduce a solution derived by Felderhof for a delta-function barrier-model [30]. In addition, we extend the calculations to angular momentum quantum numbers up to $l = 15$ and demonstrate the efficiency and accuracy of radiation boundary conditions in such calculations.

The present work is organized as follows: In Sec. II, the radiation boundary conditions are derived by the Green-function method. In Sec. III, a finite-difference representation of these boundary conditions is obtained that can be used with a standard Crank-Nicolson algorithm. In Sec. IV, the application of these boundary conditions to quantum tunneling is discussed and the validity and accuracy of the numerical procedure is thereby demonstrated. The system we investigate is a generic model of quantum tunneling, and we are able to compute the static (long-time limit) decay rates as a function of the quantum number l and the shape of the tunneling barrier. All equations will be written in atomic units such that $h/2\pi = 1, m_e = 1, q_e = -1$ (h: Planck-constant, m_e: electron mass, q_e: electron charge).

II. RADIATION BOUNDARY CONDITIONS ON THE SURFACE OF A SPHERE

The wavefunction $\psi(\boldsymbol{r},t)$ of a particle in a potential $V(\boldsymbol{r},t)$ is governed by the time-dependent Schrödinger equation (TDSE)

$$i\partial_t\psi(\boldsymbol{r},t) = \left[-\frac{1}{2}\Delta + V(\boldsymbol{r},t)\right]\psi(\boldsymbol{r},t). \qquad (1)$$

We are interested in spatially unbounded solutions that arise from a localized initial state in a localized potential. In the course of time evolution, the unbound part of the wavefunction will spread towards infinity. In most applications, the use of spherical coordinates (r,θ,ϕ), will require boundary conditions on the surface of a sphere of radius $r = R$. For definiteness, it will be assumed that both the initial wavefunction and the time-dependent potential vanish in the outside region $r > R$.

To derive radiation boundary conditions, it is sufficient to consider the evolution of the wavefunction in the outside region $r > R$,

$$i\partial_t\psi(\boldsymbol{r},t) = -\frac{1}{2}\Delta\psi(\boldsymbol{r},t), \qquad \psi(\boldsymbol{r},0) = 0. \qquad (2)$$

Expanding the angular dependence of the wavefunction in spherical harmonics

$$\psi(r,\theta,\phi,t) = \sum_{l=0}^{\infty}\sum_{m=-l}^{l}\psi_l(r,t)Y_l^m(\theta,\phi), \qquad (3)$$

yields for each angular momentum quantum number l,

$$L(r,t)\psi_l(r,t) = 0, \qquad \psi_l(r,0) = 0, \qquad r > R, \qquad (4)$$

with

$$L(r,t) = i\partial_t + \frac{1}{2r^2}\left[\partial_r r^2\partial_r - l\,(l+1)\right].$$

In the outside region, the radial wavefunctions $\psi_l(r,t)$ propagate independent of each other and independent of the azimuthal quantum number m. As a result of the partial wave expansion (3), it is sufficient to impose radiation boundary conditions on the radial wavefunctions $\psi_l(r,t)$.

We now follow the Green-function approach as described in [19, 31]. For arbitrary sufficiently smooth functions $\psi_1(r,t)$ and $\psi_2(r,t)$, the Green identity of the operator L is given by

$$\begin{aligned}&\int_0^\infty dt' \int_R^\infty dr' r'^2 \{\psi_2' L' \psi_1' - \psi_1' L'^* \psi_2'\} \\ &= \frac{1}{2}\int_0^\infty dt' r'^2 \{\psi_2' \partial_{r'}\psi_1' - \psi_1' \partial_{r'}\psi_2'\}\Big|_{r'=R}^\infty \\ &+ i\int_R^\infty dr' r'^2 \{\psi_2'\psi_1'\}\Big|_{t'=0}^\infty . \end{aligned} \tag{5}$$

where $\psi_{1,2}' = \psi_{1,2}(r',t')$, $L' = L(r',t')$, the prime denotes integration variables and the star the complex conjugate. Based on the Green identity one can obtain an integral representation of solutions of (4). For this purpose the function ψ_1 is chosen as a solution ψ_l of (4) and the function ψ_2 is replaced by the Green-function $G_l(r,r',t-t')$ that describes the propagator from a point (r',t') to a point (r,t). Because of the time-independence of the coefficients of L, the Green-function depends only on the time-difference $\tau = t - t'$. More definitely, the Green-function $G_l(r,r',\tau)$ is defined as a solution of the inhomogeneous differential equation

$$L(r',\tau)\ G_l(r,r',\tau) = \frac{R^2}{r'^2}\delta(r-r')\delta(\tau) \tag{6}$$

with $L(r',\tau)$ given by (4). It is noted that $L(r',\tau) = L^*(r',t')$ is also the operator that acts on the function ψ_2' in the Green identity (5). On the right hand side, the factor r'^{-2} accounts for the areal density of a spherical surface with radius r' and the constant factor R^2 is included for convenience. In addition the Green-function is required to satisfy the inital and boundary conditions,

$$G_l(r,r',\tau)\big|_{\tau\le 0} = 0, \tag{7a}$$

$$\partial_{r'} G_l(r,r',\tau)\big|_{r'=R} = 0, \tag{7b}$$

$$\int_0^\infty dt'\ r'^2 \{G_l \partial_{r'}\psi_l' - \psi_l' \partial_{r'} G_l\}\big|_{r'\to\infty} = 0. \tag{7c}$$

It vanishes for all times $t' \ge t$. In contrast to the more familiar Green-function for infinite space [32], the present Green-function is required to have a vanishing normal derivative on the inner spherical boundary $r' = R$ of the outside region. The last boundary condition relates the asymptotic behavior of the Green-function at infinity to that of the outgoing wave solution ψ_l.

Using the Green identity (5) with $\psi_2 = G_l$ being the Green-function (6) and $\psi_1 = \psi_l$ being a solution of (4) one obtains an integral representation for the wavefunction in the outside region in terms of the boundary values on the surface $r = R$

$$\psi_l(r,t) = \frac{1}{2}\int_0^t d\tau\ G_l(r,R,\tau)\ \partial_{r'}\psi_l(R,t-\tau), \qquad r > R.$$

Taking the limit $r \to R$ and denoting $\psi_l(r,t)|_{r=R} = f_l(t)$, $\partial_r\psi_l(r,t)|_{r=R} = g_l(t)$ one obtains a relationship between the function values $f_l(t)$ at time t and the normal derivatives $g_l(t')$ at all previous times t' on the boundary $r = R$,

$$f_l(t) = \frac{1}{2}\int_0^t d\tau\ G_l(R,R,\tau)\ g_l(t-\tau). \tag{8}$$

This is the radiation boundary condition on the spherical surface $r = R$ that can be imposed on numerical solutions for the inside region. It is expressed in terms of the Green-function $G_l(R,R,\tau)$ with both spatial points evaluated on the surface.

The Green-function will now be determined by the method of Laplace transformation. The Laplace transform $\hat{h}(\omega)$ of a function $h(t)$ with $h(t) = 0$ for $t < 0$ and $h(t) < e^{ct}$ for $t \to \infty$ will be defined as

$$\hat{h}(\omega) = \int_0^\infty dt\ h(t) e^{i\omega t}, \qquad \Im\{\omega\} \ge c. \tag{9}$$

Here we use a complex frequency ω instead of the more common complex variable $s = -i\omega$. The Laplace transform $\hat{G}_l(r,r',\omega)$ of the Green-function $G_l(r,r',\tau)$ with respect to the variable τ satisfies the ordinary differential equation,

$$\begin{aligned}\left[\frac{1}{r'^2}\partial_{r'} r'^2 \partial_{r'} + 2\omega - \frac{l(l+1)}{r'^2}\right]\hat{G}_l(r,r',\omega) \\ = 2\frac{R^2}{r'^2}\delta(r-r')\end{aligned} \tag{10}$$

with the boundary conditions

$$\begin{aligned}\partial_r' \hat{G}(r,r',\omega)\big|_{r'=R} &= 0, \\ \left.\frac{\partial_{r'}\hat{G}_l(r,r',\omega)}{\hat{G}_l(r,r',\omega)}\right|_{r'=\infty} &= \left.\frac{\partial_{r'}\hat{\psi}_l(r',\omega)}{\hat{\psi}_l(r',\omega)}\right|_{r'=\infty}.\end{aligned} \tag{11}$$

The boundary condition at infinity follows from the corresponding boundary condition in (7) with the help of the convolution theorem for the Laplace transform

$$\int_0^\infty dt e^{i\omega t}\int_0^\infty dt' f(t-t')g(t') = \hat{f}(\omega)\hat{g}(\omega),$$

where $f(t) = g(t) = 0$ for $t < 0$. In the region $r' > r$, the solutions of (10) are known as the spherical Bessel and Hankel functions [32, 33]. The particular solution that satisfies the outgoing wave condition for $\hat{\psi}_l(r',\omega)$ in (11) is

$$\hat{G}_l(r,r',\omega) = C_l(r,\omega)\ h_l^{(1)}(\rho'), \tag{12}$$

with $\rho' = kr'$, $k = \sqrt{2\omega}$ and the spherical Hankel function $h_l^{(1)}(z)$. For $|z| \to \infty$, it has the appropriate asymptotic behavior

$$h_l^{(1)}(z) \to \frac{1}{z} e^{i[z-(l+1)\pi/2]}. \tag{13}$$

The solution for $r' > r$ can be matched to a corresponding solution for the region $R < r' < r$ by using at $r = r'$ the jump conditions ,

$$\begin{aligned} \hat{G}_l(r, r', \omega)\big|_{r'=r-}^{r+} &= 0, \\ \partial_{r'} \hat{G}_l(r, r', \omega)\big|_{r'=r-}^{r+} &= 2\frac{R^2}{r^2}, \end{aligned} \tag{14}$$

where $r-$ denotes the left-side and $r+$ the right-side limit to the point r. Evaluating the jump condition at $r = R$ with the solution (12) on the right and the boundary condition (11) on the left side yields

$$C_l(R, \omega)\ k\partial_\rho h_l^{(1)}(\rho)\big|_{\rho=kR} = 2 \tag{15}$$

It follows that the Laplace transform of the Green-function $\hat{G}_l(R, R, \omega)$ on the boundary is given by the expression [19]

$$\hat{G}_l(R, R, \omega) = \frac{2}{k} \frac{h_l^{(1)}(\rho)}{\partial_\rho h_l^{(1)}(\rho)}\bigg|_{\rho=kR}. \tag{16}$$

Sometimes it is more convenient to use instead of the radial wavefunctions $\psi_l(r, t)$ the related functions $\phi_l(r, t) = r\psi_l(r, t)$, satisfying a simpler radial wave equation

$$M(r, t)\phi_l(r, t) = 0, \qquad \phi_l(r, 0) = 0, \qquad r > R, \tag{17}$$

with

$$M(r, t) = i\partial_t + \frac{1}{2}\partial_r^2 - \frac{l\,(l+1)}{2r^2}.$$

This transformation shows that the spherically symmetric three-dimensional problem can be reduced to the one-dimensional problem, except for the additional centrifugal potential for non-zero angular momentum.

The Green identity for the operator M and the corresponding integral representation of the solution ϕ_l can be derived along analogous lines. For completeness, we briefly summarize the corresponding results. The Green-function is now denoted by $H_l(r, r', \tau)$ and defined by the equations

$$M(r', \tau)H_l(r, r', \tau) = \delta(r - r')\delta(\tau), \tag{18a}$$
$$H_l(r, r', \tau) = 0, \qquad \text{for} \quad \tau \le 0, \tag{18b}$$
$$\partial_{r'} H_l(r, r', \tau)\big|_{r'=R} = 0, \tag{18c}$$
$$\int_0^\infty dt'\ \{H_l \partial_{r'}\phi_l' - \phi_l' \partial_{r'} H_l\}\,\big|_{r'\to\infty} = 0. \tag{18d}$$

The boundary values $\eta_l(t) = \phi_l(R, t)$ and $\gamma_l(t) = \partial_{r'}\phi_l(r', t')|_{r'=R}$ are related by the radiation boundary condition

$$\eta_l(t) = \frac{1}{2}\int_0^t d\tau\ H_l(R, R, \tau)\gamma_l(t - \tau), \tag{19}$$

and the Laplace transform of the Green-function $H_l(R, R, \tau)$ is given by

$$\begin{aligned} \hat{H}_l(R, R, \omega) &= \frac{2}{k} \frac{\rho\ h_l^{(1)}(\rho)}{\partial_\rho[\rho\ h_l^{(1)}(\rho)]}\bigg|_{\rho=kR} \\ &= \frac{\hat{G}_l(R, R, \omega)}{1 + \frac{1}{2R}\hat{G}_l(R, R, \omega)}. \end{aligned} \tag{20}$$

Note that both Green-functions agree in the limit $R \to \infty$ when the effects of spherical convergence become small. It is also of interest to confirm the correct behavior for zero angular momentum, $l = 0$, when the centrifugal potential vanishes. Noting that the spherical Hankel function for $l = 0$ is given by

$$h_0^{(1)}(\rho) = -\frac{i}{\rho}\ e^{i\rho} \tag{21}$$

one obtains from (16) and (20)

$$\hat{G}_0(R, R, \omega) = -\frac{2i}{k + i/R}, \tag{22a}$$
$$\hat{H}_0(R, R, \omega) = -\frac{2i}{k}, \tag{22b}$$

respectively. The Green-function $\hat{H}_0(R, R, \omega)$ is exactly the one used in previous 1d-model calculations [19]. The Green-function $\hat{G}_0(R, R, \omega)$ is related to $\hat{H}_0(R, R, \omega)$ by the transformation (20). We now consider a generalization of the Green-function approach to three dimensions with non-zero angular momentum.

In order to perform the inverse Laplace transform of (16), the spherical Hankel function $h_l^{(1)}(\rho)$ is represented in powers of $1/\rho$ by the polynomial [33]

$$h_l^{(1)}(\rho) = \frac{e^{i\rho}}{i^l}(i\rho)^{-1}\sum_{\nu=0}^{l}\left(l + \frac{1}{2}, \nu\right)(-2i\rho)^{-\nu}, \tag{23}$$

with the coefficients defined by

$$\left(l + \frac{1}{2}, \nu\right) = \frac{(l+\nu)!}{\nu!\Gamma(l - \nu + 1)}\ .$$

The derivative $\partial_\rho h_l^{(1)}(\rho)$ can similarly be represented by use of the recurrence relation [33]

$$\frac{d}{d\rho}h_l^{(1)}(\rho) = \frac{l}{\rho}h_l^{(1)}(\rho) - h_{l+1}^{(1)}(\rho). \tag{24}$$

A a result, the Laplace-transform of the Green-function (16) is obtained as a rational function of k,

$$\hat{G}_l = \frac{2}{k}\sum_{\nu=0}^{l}\left(l+\frac{1}{2},\nu\right)(-2i)^{-\nu}(kR)^{-\nu-1}\times \left[\sum_{\nu=0}^{l} l\left(l+\frac{1}{2},\nu\right)(-2i)^{-\nu}(kR)^{-\nu-2}+ i\sum_{\nu=0}^{l+1}\left(l+\frac{3}{2},\nu\right)(-2i)^{-\nu}(kR)^{-\nu-1}\right]^{-1}.$$

This rational function may be expanded in partial fractions. It turns out that for each angular momentum quantum number l there are $l+1$ simple poles,

$$\hat{G}_l(R,R,\omega) = 2\sum_{j=1}^{l+1}\frac{\alpha_j}{k-k_j}. \tag{25}$$

In the special case $l = 0$, it follows from (22a) that $\alpha_1 = -i$ and $k_1 = -i/R$. For $l > 0$, the roots k_j and coefficients α_j can be calculated numerically. A useful sum formula for the coefficients α_j is given by

$$\sum_{j=1}^{l+1}\alpha_j = -i. \tag{26}$$

It follows from the asymptotic behavior of the Green-function for large arguments, $kR \to \infty$. Using the asymptotic representation (13) and setting $k \gg k_j$ in (25) one finds

$$\hat{G}_l \to -\frac{2i}{k} = \frac{2}{k}\sum_{j=1}^{l+1}\alpha_j\ , \tag{27}$$

leading to (26).

For each pole in the representation (25), the inverse Laplace transform can readily be performed [33]. This yields the result

$$G_l(R,R,\tau) = 2\sum_{j=1}^{l+1}\alpha_j\left\{\frac{1}{\sqrt{2\pi i\tau}} - i\frac{k_j}{2}w\left(z_j\right)\right\},$$

where $z_j = -k_j\sqrt{i\tau/2}$ and

$$w(z) = e^{-z^2}\,\mathrm{erfc}(-iz)$$

is known as the complex error function. Using (26), the Green-function separates into two parts, the first of which is independent of l:

$$G_l(R,R,\tau) = \frac{-2i}{\sqrt{2\pi i\tau}} - i\sum_{j=1}^{l+1}\alpha_j k_j w\left(z_j\right) \tag{28}$$

The first part in (28) is the Green-function $H_0(R,R,\tau)$ that corresponds to the inverse Laplace transform of (22b). It is well-known from previous 1d-calculations[19]. Numerical test calculations for a free wavepacket have indicated that this one-dimensional approximation produces virtually transparent boundary conditions for $R \gtrsim 100$. For smaller computational domains, however, the full Green-function (28) should be applied at the boundary.

Some examples of the Green-function (28) are shown in Fig.1. The formula has been evaluated on a sphere with radius $R = 50$ for three different angular momentum quantum numbers $l = 0,\ 5,\ 15$. For comparison, the Green-function H_0 for a plane surface is also shown. For $l = 0$ the Green-function G_0 is slightly different from H_0 due to the differences between the radial operators (4) and (17) for a finite radius. For non-zero angular momentum the differences become more pronounced due to the presence of the centrifugal potential. With increasing angular momentum the Green-function (28) decays much faster than the one-dimensional one. It is noted that the time axis is logarithmic and therefore the characteristic relaxation time, e.g. for $l = 15$, is actually largely reduced. Truncating the integral (8) after the characteristic relaxation time of G_l may significantly reduce the numerical effort, especially for large angular momentum quantum numbers.

III. DISCRETE RADIATION BOUNDARY CONDITIONS

We now demonstrate the applicability of the radiation boundary conditions to numerical solutions of the TDSE (1) in three dimensions. For this purpose, a localized spherically symmetric potential $V(r)$ has been chosen. Using the transformation $\phi = r\psi$, and an expansion of the wavefunction with respect to spherical harmonics, the radial parts of the wave function are governed for each angular momentum quantum number l by the equation

$$\begin{aligned} i\partial_t\phi_l &= \mathcal{H}(t,r)\phi_l \\ \mathcal{H} &= \left[-\frac{1}{2}\partial_r^2 + \frac{l(l+1)}{2r^2} + V(r,t)\right]. \end{aligned} \tag{29}$$

The functions $\phi_l(r,t)$ are subject to the boundary conditions $\phi_l(r,t) = 0$ at the origin $r = 0$ and to the radiation boundary conditions (8) on the sphere $r = R$.

The numerical solution has been based on a finite-difference representation of (29) in accordance with the familiar Crank-Nicolson (CN) scheme [4]. The computational domain is represented on a grid with equidistant steps in both time and space:

$$\begin{aligned} t &= n\Delta t, & n &= 0\ldots N, \\ r &= (j+1)\Delta r, & j &= 0\ldots M. \end{aligned}$$

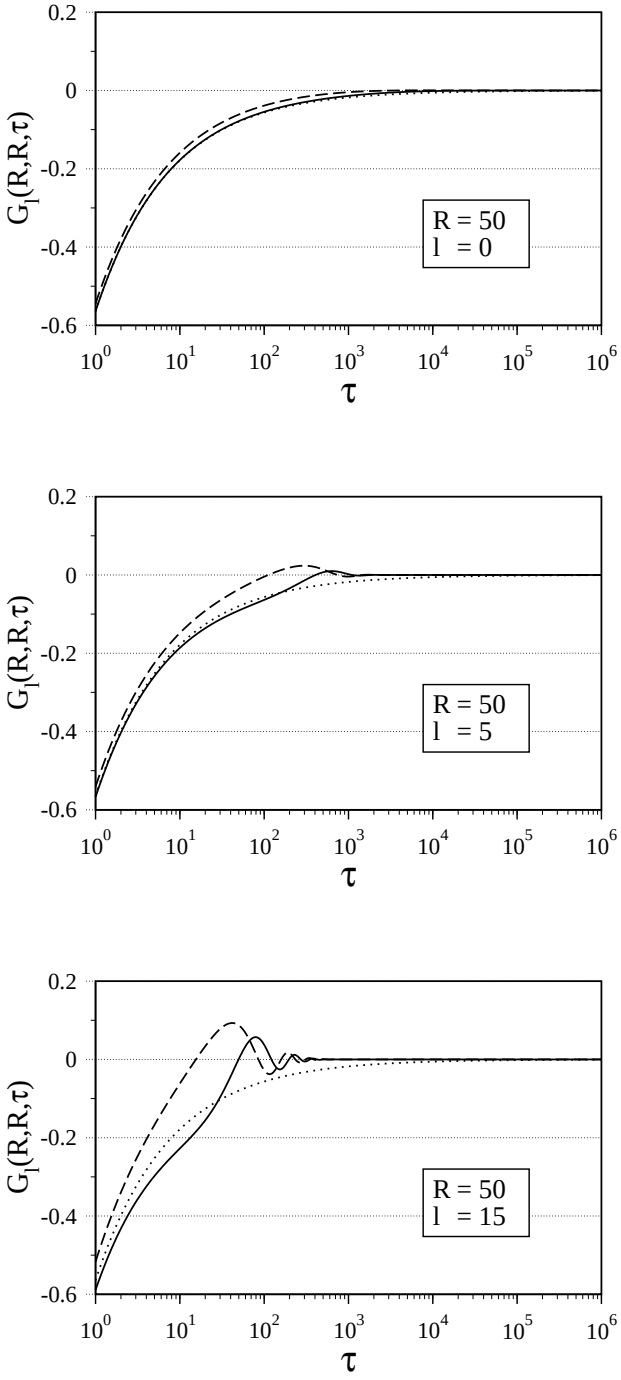

FIG. 1: Real (solid) and imaginary (dashed) part of the Green function (28) and the one-dimensional ($l-$independent) Green-function (dotted) at various values of l for $R = 50$. The real part of the one-dimensional Green-function is equal to its imaginary part.

The differential operators ∂_t and ∂_r^2 are discretized using centre-point rules. The resulting CN scheme,

$$\left(\mathbb{1} + \frac{i\Delta t}{2}\mathcal{H}^{n+1/2}\right)\phi_l^{n+1} = \left(\mathbb{1} - \frac{i\Delta t}{2}\mathcal{H}^{n+1/2}\right)\phi_l^n, \tag{30}$$

is correct up to errors quadratic in Δt and Δr. The scheme is well known to be numerically stable and to preserve the unitarity of the exact time evolution operator. The finite-difference representation of the spatial differential operator $\left(\mathbb{1} + \frac{i\Delta t}{2}\mathcal{H}^{n+1/2}\right)$ represents a tridiagonal matrix. At each time step n, the numerical solution can be computed using a LU decomposition into lower and upper triangular matrices, which in the case of tridiagonal matrices takes $\mathcal{O}(M)$ computation steps.

At the border $j = M$ of the computational domain we now have to impose the boundary condition (8) with the Green-function (28) yielding,

$$\begin{aligned} f_l(t) &= \int_0^t d\tau \frac{-i}{\sqrt{2\pi i\tau}} g_l(t-\tau) \\ &\quad + \int_0^t d\tau \mu_l(R,\tau) g_l(t-\tau), \\ \mu_l(R,\tau) &= -i\sum_{j=1}^{l+1} \alpha_j \frac{k_j}{2} w\left(-k_j\sqrt{i\frac{\tau}{2}}\right). \end{aligned} \tag{31}$$

The square root singularity in the first integral at $\tau = 0$ can be removed by a partial integration. Noting that the initial wavefunction is localized inside the region $r < R$ one obtains the more suitable form,

$$f_l(t) = \int_0^t d\tau \left(\sqrt{\frac{2i\tau}{\pi}}\,\partial_\tau + \mu_l(R,\tau)\right) g_l(t-\tau). \tag{32}$$

The numerical integration of the kernels $\mu_l(R,\tau)$ represents no basic difficulty. They are sufficiently smooth and can be computed and tabulated once in a preprocess. An example for $l = 15$ and $R = 50$ is shown in Fig.2.

To derive a finite-difference representation of this boundary condition with the same accuracy as in the CN scheme, the boundary $r = R$ is taken as the centre-point between $M\Delta r$ and $(M-1)\Delta r$,

$$\left.\begin{aligned} f_l^n &= \tfrac{\psi_l^{M,n} + \psi_l^{M-1,n}}{2} \\ g_l^n &= \tfrac{\psi_l^{M,n} - \psi_l^{M-1,n}}{\Delta r} \end{aligned}\right\} + \mathcal{O}(\Delta r^2)$$

Using the trapezoidal rule for the time integration in (32),

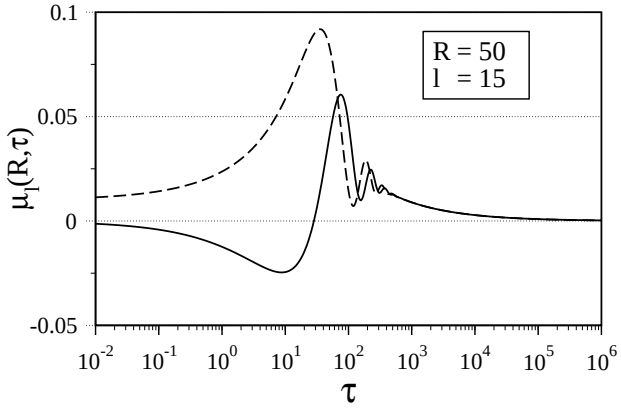

FIG. 2: Real (solid) and imaginary (dashed) part of the integral kernel $\mu_l(R,\tau)$ for $l = 15$ and $R = 50$.

one obtains the discrete boundary condition

$$\begin{aligned} B_l^n = & \left[\mathbb{1} - A - \frac{2\Delta t}{\Delta r}\mu_l^0\right]\psi_l^{M,n+1} \\ + & \left[\mathbb{1} + A + \frac{2\Delta t}{\Delta r}\mu_l^0\right]\psi_l^{M-1,n+1}, \end{aligned} \tag{33}$$

where

$$\begin{aligned} A = & \frac{-2i\sqrt{\Delta t}}{\Delta r\sqrt{2\pi i}}, \\ B_l^n = & A\left[\psi_l^{M-1,n-1} - \psi_l^{M,n-1}\right] \\ + & \frac{2\Delta t}{\Delta r}\sum_{\nu=0}^{n}\mu_l^{\nu+1}\left[\psi_l^{M,\nu} - \psi_l^{M-1,\nu}\right] \\ + & A\sum_{\nu=1}^{n-1}\sqrt{n+1-\nu}\left[\psi_l^{M,\nu+1} - \psi_l^{M-1,\nu+1}\right. \\ & \left. -\psi_l^{M,\nu-1} + \psi_l^{M-1,\nu-1}\right]. \end{aligned}$$

The boundary condition (33) couples the wavefunction on the boundary only to its nearest neighbor in space. As a result, it conserves the tridiagonal form of the CN-scheme. Also, the discretization error of the boundary condition is the same as for the Crank-Nicolson algorithm, namely $\mathcal{O}(\Delta r^2, \Delta t^2)$. Therefore, the accuracy of the overall algorithm is not affected. After the discretized kernels μ_l^ν have been computed in a preprocess, the evaluation of (33) at runtime of the program means simply a summation of $\mathcal{O}$(n) floating point numbers in each timestep n.

The computation times required with the present radiation boundary conditions can be estimated in the same manner as in [19], Eq.(2.30). For each quantum number l the total computation time T scales as

$$T = \alpha MN + \beta(N + N^2) + \gamma \tag{34}$$

where M is the number of spatial grid points, N the number of time steps and α, β, γ are numerical coefficients. The first term accounts for the inversion of the tridiagonal matrix with $\mathcal{O}(M)$ operations at each time-step, the second term for the calculation of the boundary conditions with $\mathcal{O}(\sum_{n=0}^{N} n)$ operations and the third term for other computations at the begin and end of the time integration. The computation times measured on a modern Laptop-PC follow nicely this scaling with the coefficients given by $\alpha = 8 \cdot 10^{-7}$ sec, $\beta = 1.7 \cdot 10^{-8}$ sec and $\gamma \lesssim 1$ sec. The longest calculations performed in this work, corresponding to $M = 500$ ($R = 50$ with $\Delta r = 0.1$) and $N = 2 \cdot 10^5$ ($T = 10^4$ with $\Delta t = 0.05$) require about 12 min.

Finally, it is noted that the accuracy of the radiation boundary conditions could be improved up to the accuracy $\mathcal{O}(\Delta r^4)$ at the cost of coupling the solution on the last point of the grid to its nearest and next-nearest neighbor. As a consequence, one would have to invert a matrix which is tridiagonal everywhere except in the lower-right corner, in which it would have a 3×3 block of non-vanishing values. This inversion could still be done in $\mathcal{O}(M)$ steps, provided that $M \gg 3$. This accuracy will be consistent with some improved numerical schemes for the TDSE using a Numerov method for the spatial discretization of the wavefunction[11, 13]. Another approach to improve the accuracy of radiation boundary conditions has been described in [25–28]. Here the TDSE is first discretized on an infinite domain and then boundary conditions are derived for the discrete problem, thereby avoiding any further discretization errors. In the present work, we did not follow this more rigorous approach for the reason of simplicity.

IV. QUANTUM TUNNELING THROUGH A POTENTIAL BARRIER

As an application of the present numerical method, we consider the evolution of quantum tunneling through spherically symmetric potential barriers. Recently, the long-time behavior of quantum tunneling has attracted renewed attention and an exact analytical solution of the initial-value problem for a spherically symmetric potential barrier has been obtained [30].

This work gives us the opportunity to check the results of our numerical method against an analytically known reference system. In accordance with one of the analytic models, we have chosen the initial wavefunction and the potential as

$$\phi_0(r) = \sqrt{2}\Theta(r)\Theta(1-r)\sin(\pi r), \tag{35a}$$

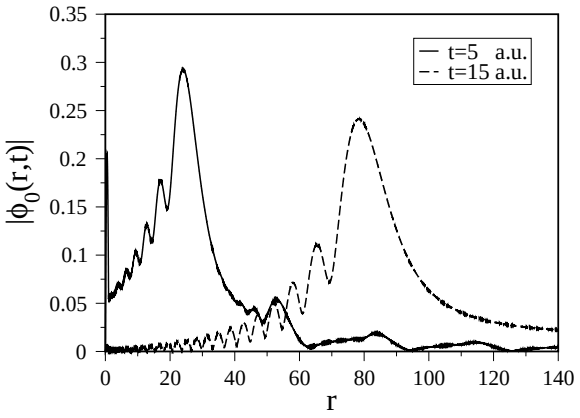

FIG. 3: Quantum tunneling of an initially localized isotropic wavefunction through a spherically symmetric delta-function potential as given by (35). At the times shown, the inital-state is already strongly depleted and a standing wave structure between the outgoing wavepacket and the potential-well has been established. The numerical result compares very well with the analytical solution from [30], Fig.3.

$$V(r) = \begin{cases} 10/w & \text{for} \quad (1-w) \le r < 1 \\ 0 & \text{elsewhere.} \end{cases} \tag{35b}$$

For $w \ll 1$, the square-well potential approaches the delta-function barrier-model used in the analytic work. We performed computations with a width $w = 0.01$. Radiation boundary conditions have been imposed at the outer border $R = \sqrt{2} \times 100$. Because of the strong confinement of the initial wavefunction and the resulting rapid phase-oscillations, a fine graining of the computational domain with $\Delta t = 5 \times 10^{-4}, \Delta r = 10^{-3}$ had to be chosen. Under these conditions, we were able to reproduce with excellent quantitative accuracy the analytical result[30]. The corresponding numerical wavefunction is shown in Fig.3. One can recognize the evolution of the outgoing wave-packet superposed by a wave reflected from the scattering center.

Having validated the numerical method for the case $l = 0$, we now proceed to the general case $l \ge 0$. As a model potential we have chosen a spherical barrier of finite height,

$$V(r) = \begin{cases} V_0 > 0 & \text{for} \quad R_1 \le r \le R_2 \\ 0 & \text{elsewhere.} \end{cases} \tag{36}$$

Inside the potential-well, the initial wavefunction $\psi_0(r)$ has been prescribed in the form

$$\psi_0 = \psi(t=0) = \exp\left[-\frac{(r-r_0)^2}{\lambda}\right] Y_l^0(\theta,\phi). \tag{37}$$

The value of λ has been adjusted in such a manner that the initial energy has always the same value E_0. The wavefunction ψ is then propagated in time using the numerical solver described in Sec. III. In several long-time computations the evolution of tunneling rates has been studied for a fixed initial energy as a function of the angular momentum quantum number.

Before looking at the physical properties of this system we have validated the quality of the discretized radiation boundary conditions. For this purpose, test calculations were carried out with identical initial wavefunctions and potentials on grids with identical discretization parameters but different spatial dimension. In the CN algorithm (30), information can travel two grid points per timestep at maximum. Therefore, if the initial wavefunction is well localized left to the potential barrier, the solution on a grid with $M \gtrsim 2N$ can be taken as a reflection-free reference. The reference solution was compared to the solutions calculated on smaller grids with radiation boundary conditions. As can be seen in Fig.4 the solutions are in perfectly good agreement even for rather small grids ($R = 50$) and large angular momenta ($l = 15$). These results are also compared with those from simpler absorbing boundaries. For this comparison, we have chosen an absorbing potential,

$$V_{abs} = -ic(r-R), \qquad R < r < 1.2 \cdot R, \tag{38}$$

with a moderate absorber thickness of $0.2 \cdot R = 10$ a.u.. The coefficient c was optimized for maximum absorption, yielding $c = 0.1$ for $l = 0$ and $c = 0.046$ for $l = 15$. The corresponding results, shown in Fig.4 by the grey line, still indicate major perturbations due to reflections from the boundary. To achieve an accuracy comparable to that with radiation boundary conditions, we had to increase the absorber thickness to about 100 a.u. in these calculations.

To gain a more quantitative measure of residual wavefunction reflection from the boundaries the final wavefunctions have been normalized to their own maximum value,

$$\psi_S(r) \equiv \psi(r, t = N\Delta t)/|\psi(r, t = N\Delta t)|_{\max}.$$

Then the difference of the scaled probability densities from the reference solution on the large grid and the solution with radiation boundary conditions on the smaller grid is evaluated,

$$\Delta|\psi_S|^2 \equiv |\psi_S|^2_{\text{Reference}} - |\psi_S|^2_{\text{RBC}}.$$

As shown in Fig.5, the deviation in the scaled probability densities actually stays very small even for long computation times.

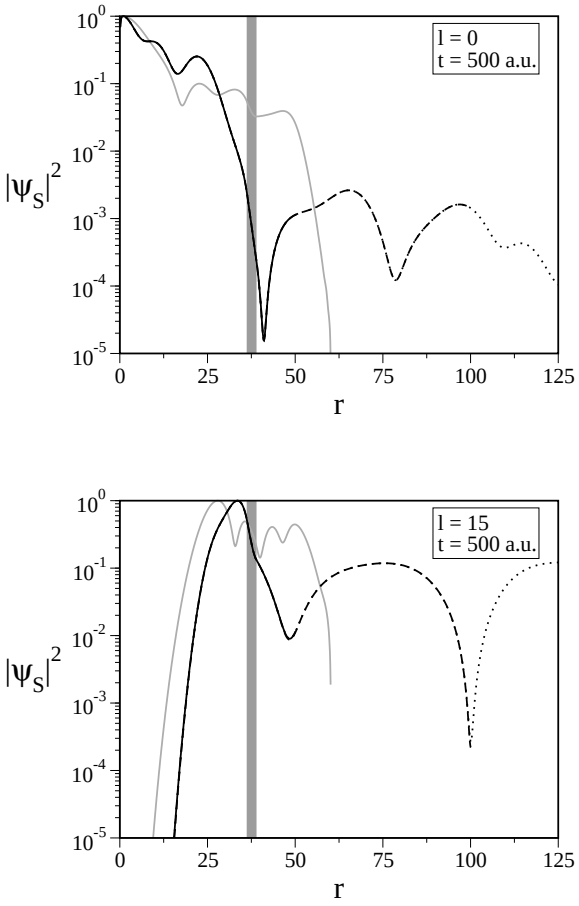

FIG. 4: Comparison of the reference solution with a boundary at $R = 2000$ (dotted) to solutions with radiation boundary conditions at $R = 50$ (solid) and $R = 100$ (dashed) and to the solution with absorbing boundary conditions in a region between $R = 50$ and $R = 60$ (grey) after 10^4 timesteps. The shaded bar indicates the position of the potential well. Simulation parameters: $E_0 = 0.5, r_0 = 25, R_1 = 36.25, R_2 = 38.75, V_0 = 0.1, \Delta t = 0.05, \Delta r = 0.1$.

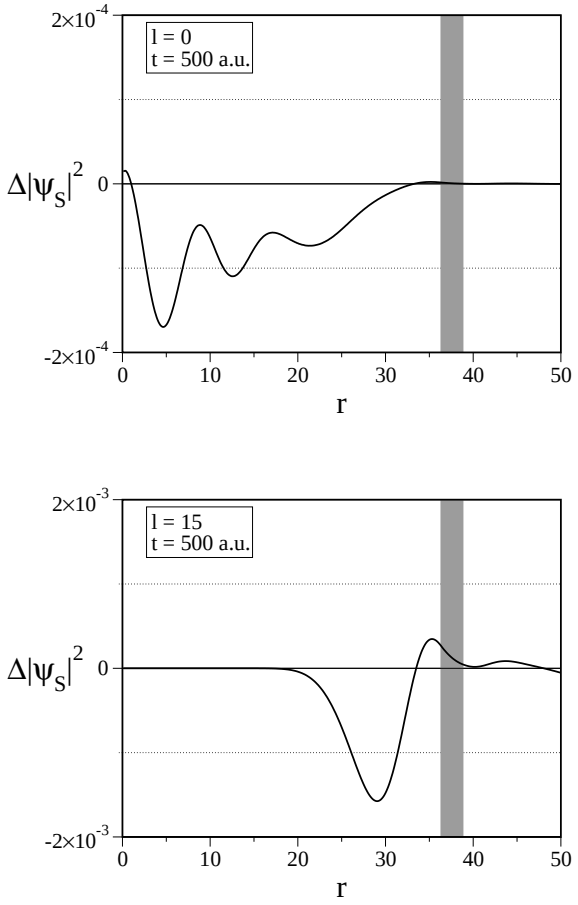

FIG. 5: The deviation in the scaled probability densities after 10^4 timesteps for radiation boundary conditions at $R = 50$. All simulation parameters are the same as in Fig. 4.

Finally, we discuss the angular dependence of tunneling rates obtained from a number of long-time simulations with radiation boundary conditions at $R = 50$. The angular momentum quantum number has been varied from $l = 0$ up to $l = 15$. Looking at the results in Figs.6-9 the following behavior can be observed.

During an initial transient phase, the wavefunction will spread out until it gets reflected back and forth by the potential barrier (36) on the one side and the centrifugal barrier $V_{eff} = l(l+1)/(2r^2)$ on the other side. In each reflection process, part of the wavefunction tunnels trough the barrier and ultimately leaves the computational domain through the open boundary. This behavior is typically observed for a few hundred atomic time units.

Gradually, the wavefunction relaxes into an exponentially decaying tunneling state with a decay rate γ_l and a static shape function $S_l(r)$:

$$\psi(t) \stackrel{t\to\infty}{\longrightarrow} c_l e^{-\gamma_l t} e^{i\omega t} S_l(r) Y_l^0(\theta, \phi). \tag{39}$$

An example of the asymptotic stationary state is shown in Fig.6 for $l = 15$.

For rising values of l, the centrifugal barrier forces the shape function S_l to localize closer and closer to the barrier, thereby enhancing the tunneling process and the static decay rate. Some examples of shape functions for different angular momentum quantum numbers l are represented in Fig.7

The approach towards a stationary state can also be recognized from the evolution of the occupation probability for the particle within the volume of the sphere $r < R$. The occupation probability P_l and the related

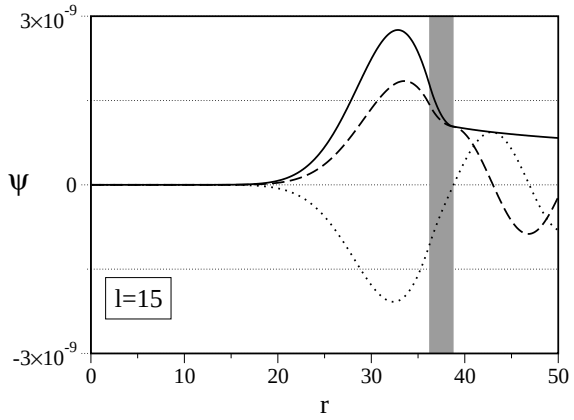

FIG. 6: A snapshot of the wavefunction for $l = 15, E_0 = 0.5, R_1 = 36.25, R_2 = 38.75, V_0 = 0.1, \Delta t = 0.05, \Delta r = 0.1$ at time $t \approx 2500$. The shaded bar shows the position of the finite potential. Dashed: real part, dotted: imaginary part, solid line: modulus.

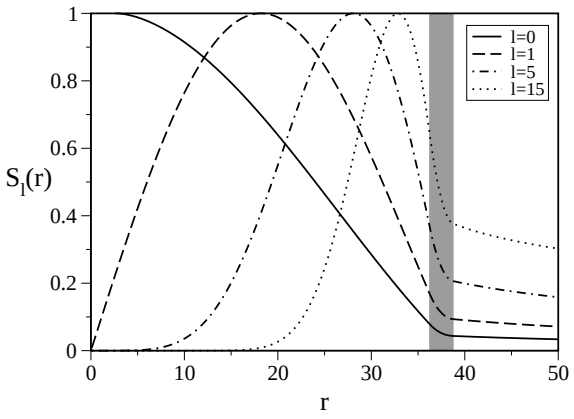

FIG. 7: Static shape functions S_l for calculations with the parameters $E_0 = 0.5, R_1 = 36.25, R_2 = 38.75, V_0 = 0.1, \Delta t = 0.05, \Delta r = 0.1$ at different values of l.

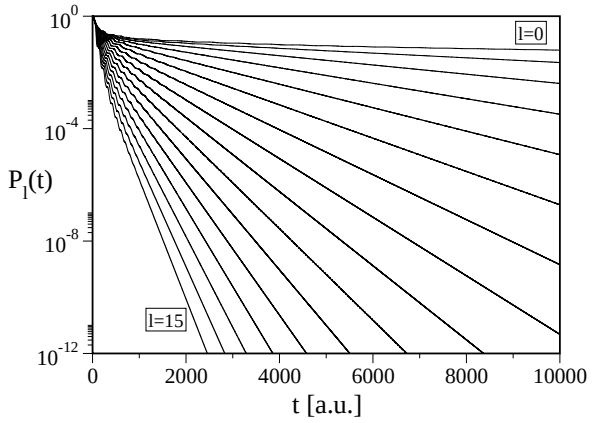

FIG. 8: Time history of the Probability P to find the particle in the computational volume. Simulation parameters: $E_0 = 0.5, R_1 = 36.25, R_2 = 38.75, V_0 = 0.1, \Delta t = 0.05, \Delta r = 0.1$. The decay rate rises with the parameter l

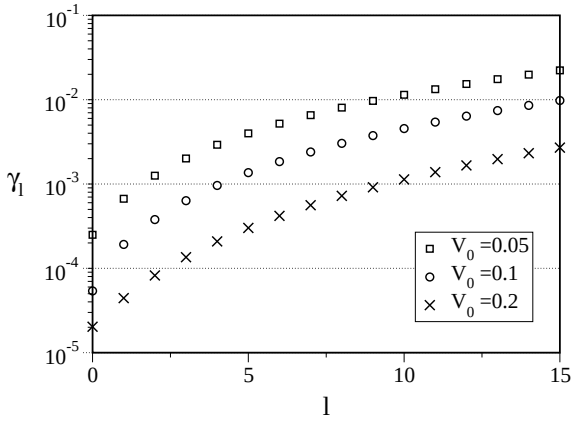

FIG. 9: Static decay rate γ_l as a function of the quantum number l for various heights V_0 of the finite barrier. Simulation parameters: $E_0 = 0.5, R_1 = 36.25, R_2 = 38.75, \Delta t = 0.05, \Delta r = 0.1$.

decay rate γ_l have been calculated as

$$P_l(t) \;=\; 4\pi \int_0^R r^2 |\psi_l(r,t)|^2 dr,$$

$$\gamma_l \;=\; -\dot{P}_l / P_l.$$

After some initial phase the occupation probability decays with a constant rate (Fig.8). The decay rate increases with the quantum number l. The dependence of the decay rate on the quantum number l and the height of the barrier is shown in Fig.9.

In summary, the use of radiation boundary conditions allows one to efficiently compute the long-time evolution of spatially unbounded quantum systems. From a generic model of quantum tunneling through a spherically symmetric potential barrier, the angular dependence of the time asymptotic tunneling rates has been obtained by this method.

V. CONCLUSION

We have given an exact analytical expression for radiation boundary conditions of the TDSE which is local in

the space of spherical harmonics $Y_l^m(\theta, \phi)$. The result is a convolution integral which maps the boundary value at time t to the history of boundary values at earlier times $t' = 0 \ldots t$. The convolution kernels show the remarkable effect of being less and less sensitive to the earlier history of the system for rising values of l, which should make it possible to truncate the convolution integral and thereby to reduce the computational effort considerably.

Our discretized version of the radiation boundary shows an error of order $(\Delta r^2, \Delta t^2)$, which is of the same magnitude as the error of the commonly used Crank-Nicolson algorithm for the solution inside the computational volume. The Numerov-algorithm, which is correct up to a higher-order in space would also be compatible with the radiation boundary conditions at the cost of inverting an almost tridiagonal matrix in each timestep.

To demonstrate the basic feasibility of the method, the computations have been restricted to spherically symmetric problems. However, it is suggested that the boundary conditions can also be applied to more general problems without spherical symmetry inside the computational volume. The only requirement is that the interaction is localized within a spherical volume. The method could also be applied in laser-atom interaction simulations if the computations were carried out in the Kramers-Henneberger reference frame, in which an electric dipole laser-field is represented by a localized (but oscillating) atomic potential.

Acknowledgement

The authors like to thank B. U. Felderhof for helpful discussions.

[1] A. Goldberg, H. M. Schey, and J. L. Schwartz, Am. J. Phys. **35**, 177 (1967).
[2] K. C. Kulander, K. R. S. Devi, and S. E. Koonin, Phys. Rev. A **25**, 2968 (1982).
[3] K. C. Kulander, Phys. Rev. A **35**, 445 (1987).
[4] J. Crank and P. Nicholson, Proc. Camb. Phil. Soc. **43**, 50 (1947).
[5] D. W. Peaceman and H. H. Rachford, Jr., SIAM J. **3**, 28 (1955).
[6] L. Lapidus and G. F. Pinder, *Numerical Solution of Partial Differential Equations in Science and Engineering* (J. Wiley, New York, 1999).
[7] M. S. Pindzola, G. J. Bottrell, and C. Bottcher, J. Opt. Soc. Am. B **7**, 659 (1990), URL `http://josab.osa.org/abstract.cfm?URI=josab-7-4-659`.
[8] M. D. Feit, J. A. Fleck, Jr., and A. Steiger, J. Comput. Phys. **47**, 412 (1982).
[9] M. E. Riley and B. Ritchie, Phys. Rev. A **59**, 3544 (1999).
[10] H. G. Muller and F. C. Kooiman, Phys. Rev. Lett. **81**, 1207 (1998).
[11] H. Muller, Laser Physics **9**, 138 (1999).
[12] E. S. Smyth, J. S. Parker, and K. Taylor, Comput. Phys. Commun. **114**, 1 (1998).
[13] D. Bauer and P. Koval, Comput. Phys. Commun. **174**, 396 (2006).
[14] H. Bachau, E. Cormier, P. Decleva, J. E. Hansen, and F. Martín, Rep. Prog. Phys. **64**, 1815 (2001).
[15] D. Neuhauser and M. Baer, J. Chem. Phys. **90**, 4351 (1989).
[16] M. S. Child, Molecular Phys. **72**, 89 (1991).
[17] C. W. McCurdy and C. K. Stroud, Comp. Phys. Comm. **63**, 323 (1991).
[18] A. Sommerfeld, Jber. der D.M.V., Leipzig **21**, 309 (1912).
[19] K. Boucke, H. Schmitz, and H.-J. Kull, Phys. Rev. A **56**, 763 (1997).
[20] M. Mangin-Brinet, J. Carbonell, and C. Gignoux, Phys. Rev. A **57**, 3245 (1998).
[21] A. M. Ermolaev, I. V. Puzynin, A. V. Selin, and S. I. Vinitsky, Phys. Rev. A **60**, 4831 (1999).
[22] E. Y. Sidky and B. D. Esry, Phys. Rev. Lett. **85**, 5086 (2000).
[23] B. Engquist and A. Majda, Math. Comput. **31**, 629 (1977).
[24] V. A. Baskakov and A. V. Popov, Wave Motion, Elsevier **14**, 123 (1991).
[25] A. Arnold, VLSI Design **6**, 313 (1998).
[26] A. Arnold, M. Ehrhardt, and I. Sofronov, Comm. Math. Sci. **1**, 501 (2003).
[27] A. Arnold, M. Ehrhardt, M. Schulte, and I. Sofronov, Matheon-Preprint **332** (2006).
[28] X. Antoine and C. Besse, J. Comput. Phys. **188**, 157 (2003).
[29] B. Alpert, L. Greengard, and T. Hagstrom, SIAM J. Numer. Anal. **37**, 1138 (2000).
[30] B. U. Felderhof, J. Phys. A **41**, 445302 (2008).
[31] E. Zauderer, *Partial differential equations of applied mathematics* (J. Wiley, New York, 1983).
[32] J. J. Sakurai, *Modern Quantum Mechanics* (Addison-Wesley, New York, 1994).
[33] M. Abramowitz and I. A. Stegun, *Handbook of Mathematical Functions* (Dover Pub., New York, 1965).